PROCEEDINGS OF ECOS 2023 - THE 36TH INTERNATIONAL CONFERENCE ON
EFFICIENCY, **C**OST, **O**PTIMIZATION, **S**IMULATION AND ENVIRONMENTAL IMPACT OF ENERGY SYSTEMS
25-30 JUNE 2023, LAS PALMAS DE GRAN CANARIA, SPAIN

Contribution of Geometric Features on the Aeroacoustic Behaviour of a Slot Diffuser

Philipp Ostmann[a], Lisa Krüger[b], Martin Kremer[b] and Dirk Müller[b]

[a] Institute for Energy Efficient Buildings and Indoor Climate, Aachen, Germany, philipp.ostmann@eonerc.rwth-aachen.de, CA
[b] Institute for Energy Efficient Buildings and Indoor Climate, Aachen, Germany, ebc-office@eonerc.rwth-aachen.de

Abstract:
Sound generated by air diffusers is a factor that affects a productive working environment and therefore plays an important role in the operation of HVAC systems. A reliable prediction of sound sources and levels offers the potential to minimise noise emissions by modifying geometric features in the early design stage of air diffusers. The research field of aeroacoustics yielded many approaches to compute not only sound propagation but also sound generation in airflows. Based on the prominent Lighthill analogy the Curle analogy and Proudman analogy were developed. In this work, we investigate a commercially available slot diffuser. The airflow through the diffuser is calculated using steady-state simulations at diffuser outlet velocities of 4, 6 and 8 m/s, which corresponds to roughly 181, 267 and 351 m^3/h, respectively. To evaluate the influence of the solid surfaces we compute the emission according to Curle's analogy. We further use Proudman's analogy to assess the effect of the freestream. Based on the flow simulation geometric optimisations are proposed. By design, a steady-state simulation is not able to capture time-resolved phenomena, such as periodic vortex shedding. But since they are far less demanding in regards to computational resources, we can simulate a wider variety of flow conditions. By identifying the primary sound source regions we not only increase the awareness towards the impact of certain flow structures, such as large scale vortex systems, but also offer a first indicator of possible design optimisations. The computed flow field is to be validated with near-field Laser-Doppler-Anemometry (LDA) measurements.

Keywords:
Aeroacoustics, Slot Diffuser, Flow Simulation, Aeroacoustics Analogy.

1. Introduction

In addition to thermal comfort, the acoustic environment also affects the general perceived comfort in buildings. Since legislation and increasing public awareness require the ventilation of public buildings, the associated acoustic emissions are gaining importance. While ventilation noise is desirable to some degree to mask other noise sources, the ventilation system should generally be as quiet as possible. The components transmitting the ventilation noise into the occupied room are air diffusers.

Typical air diffusers can be divided into two common groups: swirl and slot diffusers. In this work, we focus on the investigation of a commercially available two-slot diffuser, which is shown in Figure 1. To gain insight on the flow field, we use a detailed flow simulation which provides us the strength of acoustic sources based on a steady-state solution.

In his PhD thesis Tautz [13] performed a detailed investigation of an automotive ventilation system. He was able to reproduce not only the acoustic spectrum but also the location of the acoustic sources. The computation however required significant computational ressources.

Ravichandran et al. [11] investigated a generic automotive diffuser with disturbed inflow conditions. They used detailed transient flow simulations to compute the acoustic emissions. Although not explicitely evaluated, the main features contributing to the acoustic emissions were the guiding flaps inside the diffuser.

Kusyumov et al. [7] succesfully applied a steady-state simulation to an isolated helicopter fuselage to predict broadband noise sources. Their case included Mach numbers greater than in our case, but it demonstrates the ability of Proudman's model to predict noise emissions.

For a generic slot diffuser we already showed, that the main acoustic sources are located near sharp edges [9]. Here a steady-state simulation indicated the same regions as a transient simulation. Therefore we deem it possible to identify the main noise source regions by steady-state simulations, if the spectral distribution of the noise is not of greater interest.

Although some researchers have adressed the acoustic emissions of air diffusers in the automotive sector, a

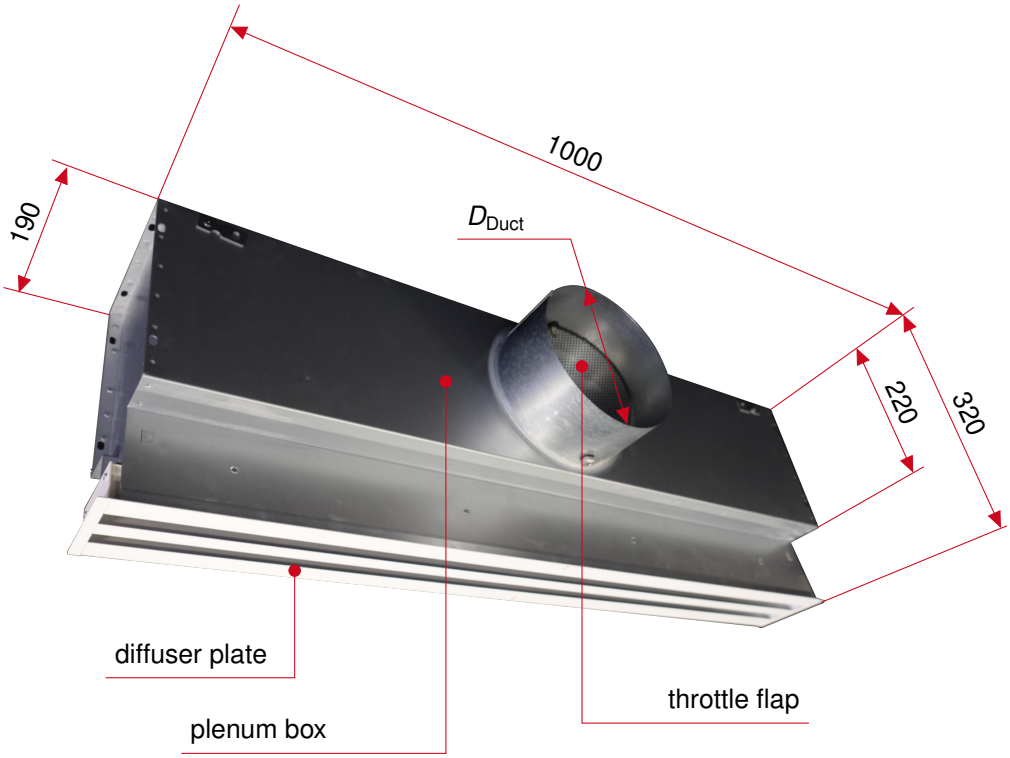

Figure 1: Picture of the investigated diffuser, dimensions given in mm

detailed investigation of the acoustic emissions of air diffusers applied in buildings have not been investigated. In this work we aim to investigate the acoustic behaviour of a slot diffuser while reducing the computational cost to locate the geometric features mainly responsible for the acoustic emission. A transient simulation offers a detailed investigation of acoustic phenomena (see [11, 13]). However the lower fidelity of a steady-state simulation is sufficient, if one is only interested in determining the main source locations (see [7, 9]).

2. Methodology

In this section we first describe the geometry of the slot diffuser and explain certain simplifications we made. We then explain the numerical and experimental setup, where the latter is needed to validate our simulations. We then present our method to rate the broadband noise emission. The slot diffuser is investigated at three diffuser outlet velocities $v_D = 4$, 6 and 8 m/s, which correspond to volume flow rates of $\dot{V} = 181$, 267 and 351 m^3/h. The diffuser outlet velocity is defined as the maximum occuring velocity within the diffuser.

2.1. Description of the geometry

Figure 1 shows the slot diffuser consisting of a circular connection duct with diameter D_{Duct}, that is connected to a plenum box. In order to limit the volume flow, an additional, perforated throttle flap is implemented in the connecting section between duct and plenum box. Preliminary simulations show, that the perforation has a negligible impact on the flow and aeroacoustic results, which is why we simplify the throttle flap by a solid round plate. The beams visible in Figure 2a, which are required to attach the diffuser plate to the plenum box, are also omitted to reduce the model size. Using the length of the plenum box l_{Plenum}, the diffuser plate features two rectangular slots with length $l_{Slot} = l_{Plenum}$ and width b_{Slot} (see Fig. 2c). Both slot channels are separated by a wall (see Fig. 2b), resulting in a total diffuser width of $b_{diffuser}$.

To alter the outlet flow pattern, both slots feature adjustable flaps, which are visible in Figure 2b. By changing the flap angle α_{Flap}, the exit flow angle can be varied between a ceiling-attached or ceiling-normal direction. In our study we only investigate the ceiling-attached case, since this is the most common setting. The geometric parameters are summarised in Table 1 and a detailed view of the simplified geometry used for the simulation is shown in Figure 2c.

2.2. Modelling of the flow and broadband noise

The slot diffuser is modelled in the commercially available software package STAR-CCM+ (17.06.008) from Siemens [12]. Although acoustic phenomena are by definition of transient nature, several models have been developed in the past to capture at least the acoustic sources from steady-state simulations. The use of

Table 1: Geometric parameters of the prepared slot diffuser

Parameter	Value	Unit	Description
D_{Duct}	198	mm	Connection duct diameter
l_{Slot}	997	mm	Length of the rectangular slots
b_{Slot}	20.5	mm	Width of one rectangular slot
α_{Flap}	43.5	°	Angle of the slot flaps

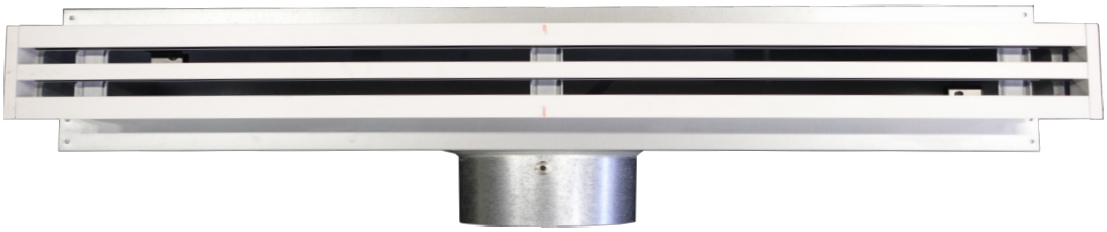

(a) View normal to the outlet of the diffuser

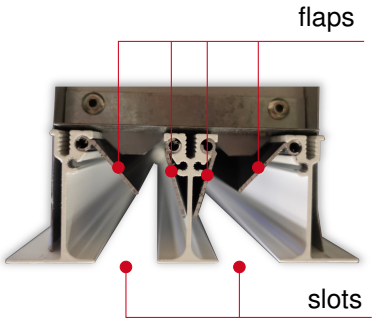

(b) Picture of the diffuser plate

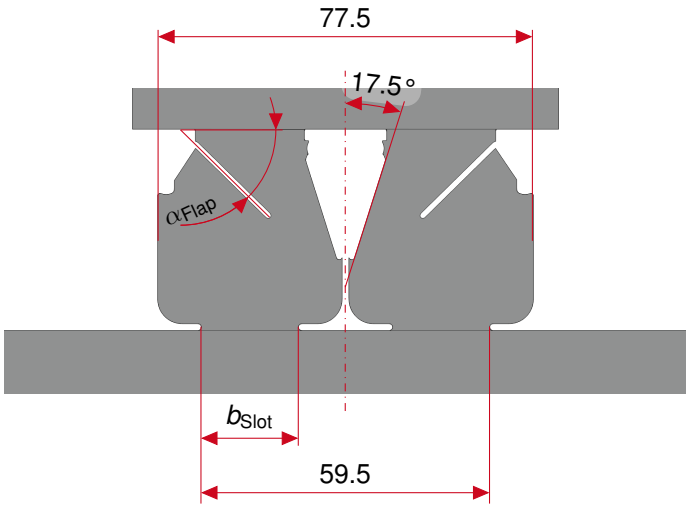

(c) Prepared geometry for the simulation model, dimensions in mm

Figure 2: Detail view of the diffuser outlet region

steady-state simulations offers significant savings in computational effort.

To accurately resolve all important geometric features, we employ an unstructured polyhedral mesh with a resolution up to $\Delta = 0.25\,\text{mm}$ near the curvatures of the flaps. Inside the plenum, the average resolution is kept close to $\Delta \approx 1.5\,\text{mm}$. We resolve the boundary layer with $n_{\text{Prism}} = 7$ prism layers with a total thickness of $\Delta_{\text{Prism}} = 2\,\text{mm}$ which results in $y^+ < 1$ in all important areas. To prevent steep gradients of mesh resolution, we set both the surface and the volumetric growth rate to 1.05. The total mesh size is $n_{\text{Cells}} \approx 61 \cdot 10^6$ cells. We use the same mesh for all simulations, since only the inlet mass flow changes.

We assume the air flow to be incompressible with a constant density ρ (see Tab. 2). The steady-state simulation is computed using a segregated flow solver. We use a pressure-velocity coupling scheme (SIMPLE), which is designated for incompressible flows [12]. In addition to incompressibility, we assume the air to be isothermal. As turbulence model we select the realizable $k-\varepsilon$ - model with all y+ wall treatment, since in our case it gives a more accurate solution of the ceiling-attached flow than e.g. the $k-\omega$ - model.

We define the inlet boundary condition with a constant mass flow condition $\dot{m} = \rho \cdot \dot{V}$ and low turbulence intensity v'/v (see Tab. 2). The diffuser is connected to a large volume which represents part of a room. While the ceiling is modelled as a no-slip wall, the other faces of the room are modelled as a pressure outlet with $p_{\text{out}} = 0\,\text{Pa}$.

Two broadband noise source models are used to calculate the aeroacoustic sources. The first model computes

broadband noise from dipole sources as a surface acoustic power P^{a}_{Curle}, which are most dominant in the vicinity of solid boundaries. It evaluates the turbulent boundary layer and was first developed by Curle [2, 3] based on the work of Lighthill [8].

$$P^{a}_{\text{Curle}} = \frac{1}{12\,\pi\overline{\rho}\overline{c}^{3}} \cdot 4\pi^{3}\,\overline{(u')^{2}}\,\left(p'_{\text{Wall}}\right)^{2} \tag{1}$$

The fluctuations $\overline{(u')^{2}}$ and p'_{Wall} can be further simplified according to Hinze [6, pp. 668-680]. The simplification yields expressions that only depend on the turbulent kinetic energy k and the wall shear stress τ_{Wall}.

$$\overline{(u')^{2}} = \frac{2}{3}\max\left(k;\ \frac{3.3\,\tau_{\text{Wall}}}{\overline{\rho}}\right) \qquad \left(p'_{\text{Wall}}\right)^{2} = \max\left(3\,\tau_{\text{Wall}};\ 0.7\,\overline{\rho}\cdot\frac{2}{3}k\right)$$

The second model was developed by Proudman [10] based on the work of Lighthill [8] and computes broadband noise from quadrupole sources originating from free stream turbulence as a volumetric acoustic power P^{a}_{Proudman}. Here u_t and L are the turbulent scales for the velocity and length.

$$P^{a}_{\text{Proudman}} = \alpha\rho\frac{\left(\overline{u_t}^{2}\right)^{4}}{c^{5}\,L} = \alpha\rho\frac{\overline{u_t}^{3}}{L}\frac{\overline{u_t}^{5}}{c^{5}} \qquad \text{with } u_t = \sqrt{\frac{2}{3}k} \tag{2}$$

Both models assume isotropic turbulence, which is consistent with turbulence modelling assumptions.

2.3. Laser-Doppler-Anemometry setup

We use a 3D-LDA system from *Dantec* that consists of a 2D *FiberFlow* and a 1D *FlowLite* probe. With proper arrangment both probes form a 3D-setup that allows us to measure all three velocity components. All optical measurements are performed in a separate chamber, which allows for a completely dark environment. The required volume flow *dotV* is delivered by a supply unit located outside of the chamber. We calculate the volume flow by measuring the pressure drop over an orifice. This method is calibrated by using a reference orifice as specified in DIN EN ISO 5167 - 2.

A schematic view of the setup in the chamber is given in Figure 3a. The diffuser is fed with air by utilising existing openings in the chamber walls to allow a connection to the supply unit. When feeding the required DEHS particles the chamber quickly fills up with fog, which renders the LDA system unable to produce good results. To mitigate this problem, we install a special exhaust system that provides an additional volume flow $\dot{V}_{\text{ex}} > 1200\,\text{m}^3/\text{h}$ to ventilate the whole chamber (depicted by → in Fig. 3a). The exhaust system draws air from the test hall environment outside the chamber through an opening in the chamber ceiling. It is then distributed using a suspended ceiling such that the exhaust volume flow is guided downwards along the chamber wall until it is captured by the exhaust hoods. We use 12 hoods that are evenly distributed around the diffuser frame. All hoods feed into a collection plenum below the frame from which an additional fan draws the exhaust volume flow. The exhaust system ensures, that the LDA probes have clear sight on the target location and no fog accumulates during the course of the whole measurement.

The 2D probe is connected to a laser which generates wavelengths of 488 nm (blue laser) and 514.5 nm (green laser), while the 1D probe utilises a laser with a wavelength of 532 nm (green laser). Each velocity component is recorded separately in non-coincident mode, since a measurement in coincident mode requires much more time to acquire a sufficient number of samples. We use beam expanders to allow the mounting of lenses with a focal length of $f_{\text{LDA}} = 500\,\text{mm}$. We attach the probes to a movable traverse system, which allows us to automatically measure a wide range of locations. Both probes are aligned along the z-direction of the diffuser with an angle of $\alpha_{\text{LDA}} = 15°$ and therefore enclose an angle of 30°. We further tilt the whole probe system by $\beta_{\text{LDA}} = 15°$ to allow for a measurement at $y = 0\,\text{mm}$. The diffuser coordinate system, that we use in this paper, is colored red in Figure 3b.

Table 2: Parameters of the flow and aeroacoustic models

Parameter	Value	Unit	Description
ρ	1.18415	$\text{kg}\,\text{m}^{-3}$	Density of the air
T	25	°C	Temperature of the air
v'/v	0.01	-	Inlet turbulence intensity
c	343	$\text{m}\,\text{s}^{-1}$	Speed of sound
$P_{\text{ac,ref}}$	$1 \cdot 10^{-12}$	W	Reference value of the acoustic power

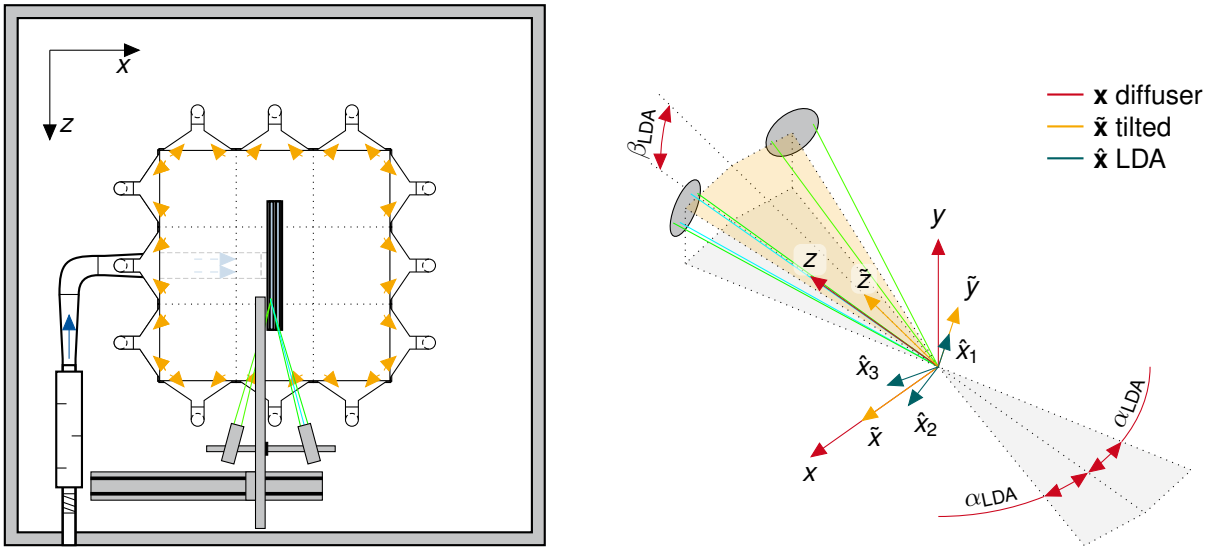

(a) Schematic of the LDA setup in the measurement chamber

(b) Sketch of the coordinate transformation

Figure 3: Setup of the LDA measurement and definition of the diffuser coordinate system

For each measured velocity component u_i, we acquire $N_i \geq 5000$ samples over a maximum duration of 5 min per evaluation point. The averages are calculated by using the arithmetic average, where $N_1 \neq N_2 \neq N_3$ due to non-coincident measurement.

$$\overline{u_i} = \frac{1}{N_i} \sum_{k=1}^{N_i} u_i(k) \tag{3}$$

To calculate the velocity components within the diffuser coordinate system $\mathbf{x} = (x, y, z)$, two transformations are required. A sketch of the coordinate transformations is given in Figure 3b. The first transformation $\mathbf{A}$ is used to translate the probe signals from their coordinate system $\hat{\mathbf{x}} = (\hat{x}_1, \hat{x}_2, \hat{x}_3)$ into a tilted, intermediate coordinate system $\tilde{\mathbf{x}} = (\tilde{x}, \tilde{y}, \tilde{z})$.

The blue laser (488 nm) is oriented vertically and measures u_1. Both green lasers (514.5 nm and 532 nm) are aligned horizontally and measure u_2 and u_3 respectively. We then apply another rotation transformation $\mathbf{B}$ about the $\tilde{x}$-axis to acquire the velocity components in the diffuser coordinate system.

$$\tilde{\mathbf{x}} = \mathbf{A} \cdot \hat{\mathbf{x}} \quad \text{, with } \mathbf{A} = \begin{bmatrix} 0 & \frac{1}{2\cos(\alpha_{\mathrm{LDA}})} & \frac{1}{2\cos(\alpha_{\mathrm{LDA}})} \\ 1 & 0 & 0 \\ 0 & -\frac{1}{2\sin(\alpha_{\mathrm{LDA}})} & \frac{1}{2\sin(\alpha_{\mathrm{LDA}})} \end{bmatrix} \tag{4}$$

$$\mathbf{x} = \mathbf{B} \cdot \tilde{\mathbf{x}} \quad \text{, with } \mathbf{B} = \begin{bmatrix} 1 & 0 & 0 \\ 0 & \cos(\beta_{\mathrm{LDA}}) & -\sin(\beta_{\mathrm{LDA}}) \\ 0 & \sin(\beta_{\mathrm{LDA}}) & \cos(\beta_{\mathrm{LDA}}) \end{bmatrix} \tag{5}$$

$$\mathbf{x} = \mathbf{B} \cdot \mathbf{A} \cdot \hat{\mathbf{x}} = \mathbf{C} \cdot \hat{\mathbf{x}} \tag{6}$$

We use the combined transformation matrix $\mathbf{C}$ to transform the velocity components and their respective variances.

2.4. Validation of the computed flow-field

To validate the flow field, the computed average velocity magnitude $\overline{|\mathbf{v}|}$ and the turbulent kinetic energy (TKE) k are compared with the LDA measurements. The steady-state simulation calculates time-averaged results only but directly reports the necessary values for $\overline{|\mathbf{v}|}$ and k.

In the case of the LDA measurements both values need to be computed from the recorded samples. For the velocity components, we can directly apply the coordinate transformation from equation 6 to the averaged probe signals $\overline{u}_{\mathrm{LDA}} = (\overline{u}_1, \overline{u}_2, \overline{u}_3)$.

$$\overline{\mathbf{v}} = \mathbf{C} \cdot \overline{u}_{\mathrm{LDA}} \tag{7}$$

Since we measure the variance of the velocity in the skewed LDA-coordinate system, we need to apply the transformation directly to the measured values. The transformation of the variances of u_i onto the x-direction

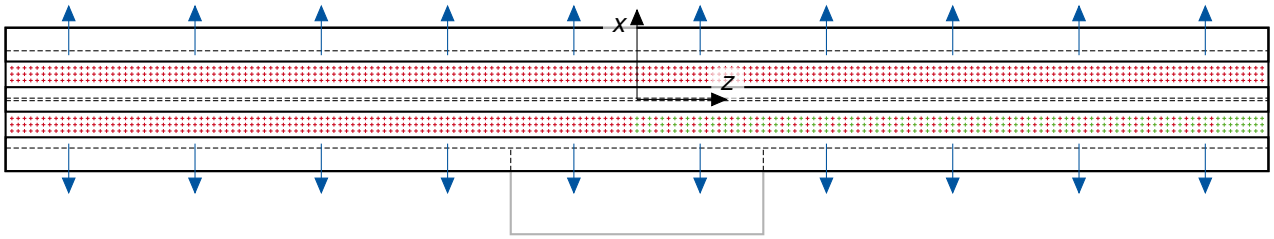

Figure 4: Evaluation points for the velocity field validation (green: LDA, red CFD)

is illustrated by equation 8, the other velocity components are treated similarly.

$$\overline{v_x'^2} = \left[\frac{1}{N_1}\sum_{i=1}^{N_1}\Big((u_1(i)-\overline{u_1})\cdot c_{11}\Big)^2\right] + \left[\frac{1}{N_2}\sum_{j=1}^{N_2}\Big((u_2(j)-\overline{u_2})\cdot c_{12}\Big)^2\right] + \left[\frac{1}{N_3}\sum_{k=1}^{N_3}\Big((u_3(k)-\overline{u_3})\cdot c_{13}\Big)^2\right] \tag{8}$$

Since the data rate for a full or semi-coincident measurement is too low, we are however not able to validate this approach yet. Finally, we use the transformed values to calculate the average velocity magnitude $\overline{|\mathbf{v}|}$ and TKE k according to equations 9 and 10.

$$\overline{|\mathbf{v}|} = \sqrt{\overline{v_x}^2 + \overline{v_y}^2 + \overline{v_z}^2} \tag{9}$$

$$k = \frac{1}{2}\left(\overline{v_x'^2} + \overline{v_y'^2} + \overline{v_z'^2}\right) \tag{10}$$

We validate the flow-field on the diffuser outlet plane at specific points on a x-z-plane at $y = 0\,\mathrm{mm}$. We spatially discretise the outlet section by $\Delta x = \Delta y = 5\,\mathrm{mm}$. The positioning of the validation points is displayed in Figure 4. Due to the limited spatial range of the LDA traverse system, we only measure points below $x < 0$ and above $z \geq 0$. We further reduce the number of points to be measured by downsampling the points towards the centre of the outlet and investigating only one slot. This is applicable as the flow field is symmetrical. Consequently, we measure the green points + with LDA. In the simulation, we additionally capture all red points +. In total, the outlet is discretised by 1194 points, of which 162 are measured with LDA.

The manufacturer's data sheet specifies certain operating points which are you used to validate the total-to-static pressure drop between the diffuser inlet $p_{\mathrm{tot,in}}$ and the ambient pressure in the chamber $p_{\mathrm{st,amb}}$. The inlet pressure is measured at the same section for the simulation and the experiment.

$$p_{\mathrm{tot,in}} = p_{\mathrm{st,in}} + \frac{\rho}{2}v^2 \tag{11}$$

$$\Delta p = p_{\mathrm{tot,in}} - p_{\mathrm{st,amb}} \tag{12}$$

Since the volume flow rates given in the data sheet do not match the simulated flow rates, the pressure drop is approximated.

$$\Delta p_{\xi,x} = \xi \cdot \dot{V}^x \tag{13}$$

$$\min \sum_{i=1}^{N}\left(\frac{\Delta p_{\mathrm{data}} - \Delta p_{\xi,x}}{\Delta p_{\mathrm{data}}}\right)^2 \tag{14}$$

The pressure loss coefficient ξ and the exponent x are calulated by using a regression model, which minimises the sum of the squared errors. Using $\xi = 4.18 \cdot 10^{-4}$ and $x = 1.91$, we can approximate the data sheet values with a maximum relative error of MAE = $4.195 \cdot 10^{-2}$. By using the approximated pressure $\Delta p_{\xi,x}$ we can assess the error of the flow model regarding the pressure losses at the respective volume flow $\dot{V}$.

$$\Delta p_{\mathrm{error}} = \frac{\Delta p_{\mathrm{sim}}(\dot{V}) - \Delta p_{\xi,x}(\dot{V})}{\Delta p_{\xi,x}(\dot{V})} \tag{15}$$

2.5. Evaluation of aeroacoustic broadband noise

To evaluate the total broadband noise predicted by both aeroacoustic broadband noise models, we integrate their respective acoustic power values. The Curle model predicts noise emitted from surfaces, which is why we integrate its power on representative boundary surfaces (see Fig. 5a). Since Proudman's model computes

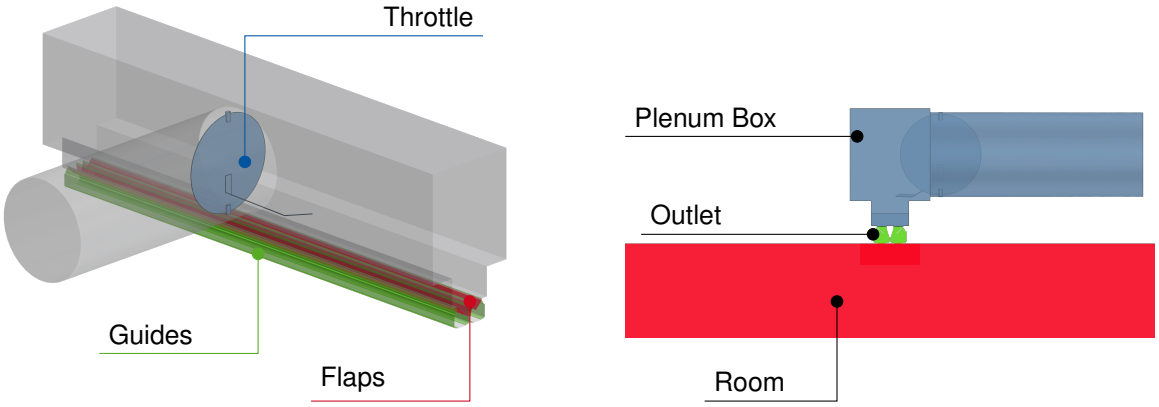

(a) Evaluation surfaces for the Curle calculation

(b) Evaluation volumes for the Proudman calculation

Figure 5: View on the surfaces and volumes used for the aeroacoustic broadband noise evaluation

a volumetric acoustic power, we apply a volume integral to specific subregions of interest (see Fig. 5b).

$$P_{\text{int,Curle}} = \int_S P^{\text{a}}_{\text{Curle}} \cdot ds \tag{16}$$

$$P_{\text{int,Proudman}} = \int_V P^{\text{a}}_{\text{Proudman}} \cdot dv \tag{17}$$

All integrated acoustic powers are then converted into the dB scale using the reference value $P_{\text{ac,ref}}$ (see Tab. 2).

$$P_{\text{ac,Curle/Proudman}} = 10 \cdot \log_{10}\left(\frac{P_{\text{int,Curle/Proudman}}}{P_{\text{ac,ref}}}\right) \tag{18}$$

By comparing the individual subsets, we can assign high noise emissions to individual geometric features. The selected subsets are shown in Figure 5. To evaluate the acoustic emissions from solid boundaries with Curle's model, we select three boundary subsets (see Fig. 5a). We further define three volumes in which we evalute the emissions from Proudman's model (see Fig. 5b). In both cases we also evaluate the overall emission from all boundaries (including the plenum box and the ceiling) and from the entire fluid region.

3. Results

We give a detailed discussion and validation of the results for the medium diffuser velocity $v_{\text{D}} = 6\,\text{m/s}$ which corresponds to a volume flow of $\dot{V} = 267\,\text{m}^3/\text{h}$.

3.1. Flow field validation

To validate the flow field we reduce the evaluation to the half of the lower slot ($x < 0, z > 0$) that was measured with LDA (see Sec. 2.3.). The sampled fields are shown in Figure 6 with their respective available spatial sampling resolution (see Sec. 2.4.).

By applying the sampling we calculate the computed average velocity to $|\overline{v}|_{\text{avg,CFD}} = 4.13\,\text{m/s}$, which is slightly higher than the measured value of $|\overline{v}|_{\text{avg,LDA}} = 3.80\,\text{m/s}$. The relative deviation of the average velocity is $|\overline{v}|_{\text{avg,CFD}}/|\overline{v}|_{\text{avg,LDA}} < 8\,\%$. The maximum values are $|\overline{v}|_{\text{max,CFD}} = 5.13\,\text{m/s}$ and $|\overline{v}|_{\text{max,LDA}} = 4.75\,\text{m/s}$ respectively. Although we set the same volume flow rates in both simulation and measurement, small leakages in the ducting system and non-airtight edges of the diffuser may have contributed to discrepancies between our computed and measured results. In addition to the influence of the inlet duct, the beams inside the diffuser plenum box (see Fig. 2a) cause significant distortions in the flow field. In the centre and near the edge the wake is clearly visible by considerably lower velocities. Since the beams are neglected in the simulation setup, this leads to a significant local deviation. We still consider the computed velocity field to be valid, given the fact, that the beams are neglected. The overall lower average velocity in the measurement is explained by leakages in the measurement setup.

The sampled measured and computed TKE distributions are shown in Figure 7. We observe considerably higher measured levels than in the simulation. Again the wake of the beams is clearly notable, but even in the area between the beams the measured TKE values are approximately doubled. By design the simulation assumes isotropic turbulence ($v_{\text{x}}'^2 = v_{\text{y}}'^2 = v_{\text{z}}'^2$). However, the measurements show a strong anisotropic

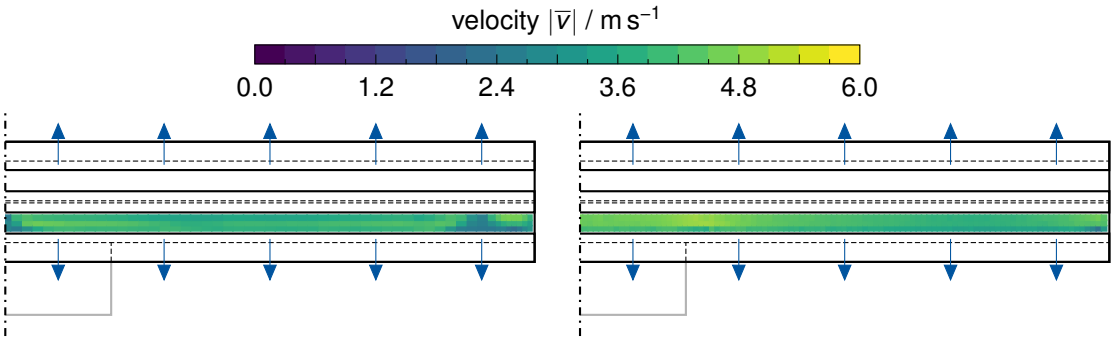

(a) Measured flow field (b) Computed flow field

Figure 6: Velocity field

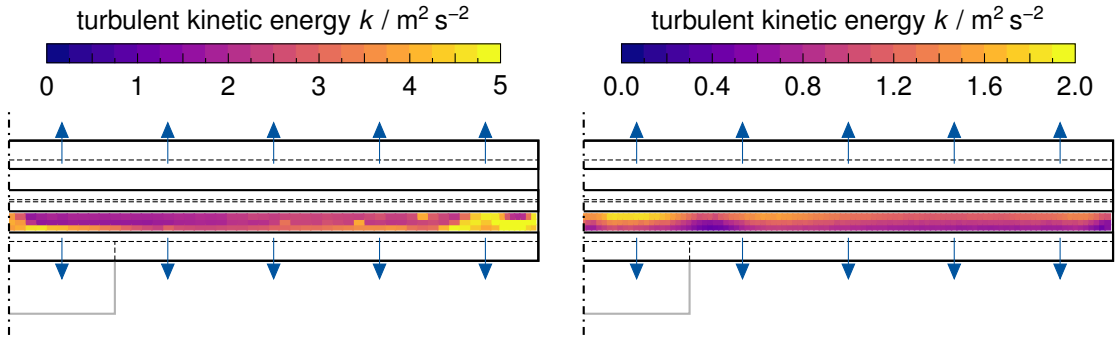

(a) Measured turbulent kinetic energy (b) Computed turbulent kinetic energy

Figure 7: Turbulent kinetic energy

behaviour. In our case the variance in z-direction is almost an order of magnitude higher higher than in the other directions ($v_z'^2 \gg v_y'^2 > v_x'^2$). Overall, the measured kinetic energy is higher than in the simulation and the impact of the beam wakes prevent a proper validation of the turbulence.

As an additional metric, we also assess the pressure drop across the diffuser. In Figure 8 the pressure drop Δp is plotted against the volume flow $\dot{V}$. The solid lines indicate the regression model as explained in Section 2.4. and the points represent the individual values. The evaluation shows no significant difference between the measured and simulated pressure drop. Furthermore the regression model shows practically the same slope over the investigated volume flow range. Since the measured and computed pressure drop is practically equal, we only summarise the data sheet and the computed values in Table 3. The data sheet reports a higher pressure drop than measured and computed but also shows a comparable slope. Since the setup used by the manufacturer to assess the pressure drop is unknown, the slightly higher values might be due to other ambient air conditions or differences in the setup. We consider the pressure drop and therefore the wall shear stresses τ_{Wall} to be valid as well, because the pressure drop of our measurement and simulation match (see Fig. 8)

In conclusion, we deem our simulation to be valid in regards to the averaged velocity field and the overall pressure drop across the diffuser. We compute significantly lower turbulence levels. In large parts we account this to the assumption of isotropic turbulence by the $k-\varepsilon$ - model. Another factor might be, that we achieve higher turbulence intensities at the diffuser inlet in our measurements. Since the computation of Curle's model is mainly defined by the wall shear stress instead of the low turbulent kinetic energy in the boundary layer (see eq. 1), we deem it's results sufficiently accurate.

Figure 9 shows the computed flow field on two sections through the whole diffuser which originate at $(x, y, z) = (0, 0, 0)$. The flow exits the diffuser at an angle of $\approx 40°$ and attaches to the ceiling shortly after exit, as can be seen in Figure 9a. The maximum diffuser velocity of $v_D = 6\,\text{m/s}$ occurs in the vicinity of the flaps at $y \approx -15\,\text{mm}$. The velocity field shown in Figure 9b is inhomogeneous, although it is nearly symmetric along the x-axis. The maximum velocity at the outlet plane is lower than the diffuser velocity ($|\overline{v}|_{\text{max},y=0} = 5.24\,\text{m/s} < v_D$), which can be attributed to the larger cross-sectional area available for the flow. By averaging the velocity in the outlet section, we can calculate the relative average velocity, which is roughly constant across all investigated

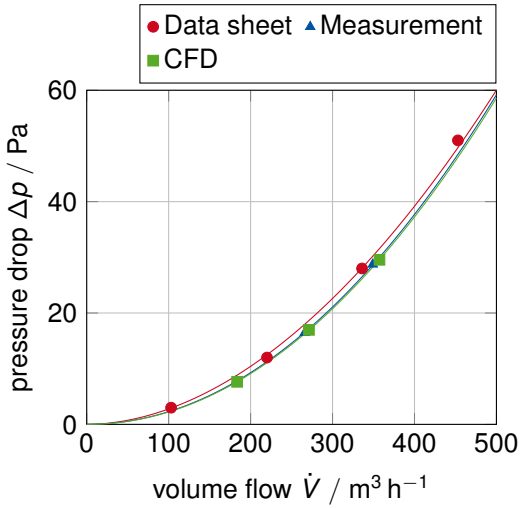

Figure 8: Validation of the pressure drop

Table 3: Overview of Δp_{error} values for the three computed volume flows

volume flow $\dot{V}$ m³/h	$\Delta p_{\xi,x}$ Pa	Δp_{sim} Pa	Δp_{error} %
184	8.8	7.6	−13.5
271	18.6	17.0	−9.0
357	31.6	29.6	−6.4

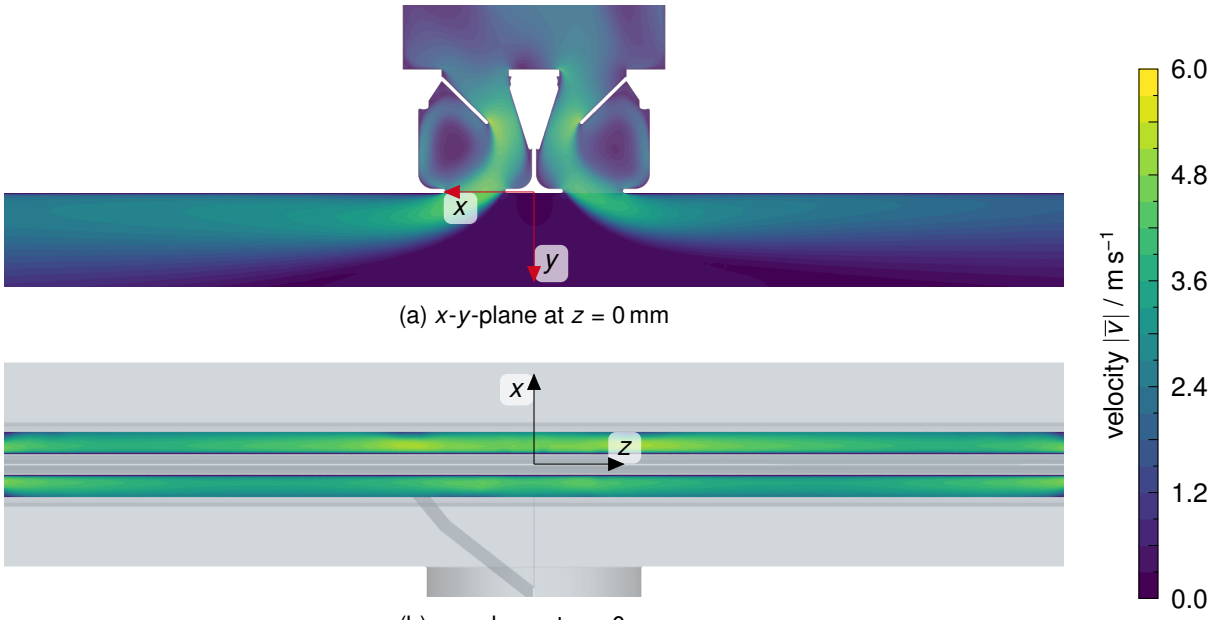

(a) x-y-plane at $z = 0\,\text{mm}$

(b) x-z-plane at $y = 0\,\text{mm}$

Figure 9: Computed velocity field for $v_{\text{D}} = 6\,\text{m/s}$

diffuser velocities.

$$\frac{|\overline{v}|_{\text{avg},y=0}}{v_{\text{D}}} = \frac{3.46\,\text{m/s}}{6\,\text{m/s}} = 0.58 \approx \text{const.} \tag{19}$$

Especially in the centre of the diffuser ($-150\,\text{mm} < z < 150\,\text{mm}$) the inflow duct has a great impact on the flow field. The areas where high velocities occur in the upper slot ($x > 0$) are further spread apart ($|z| \uparrow$). We do not observe the same spread distribution in the lower slot ($x < 0$), where multiple areas of roughly equal velocity are located near the centre and near the outer edges.

Figure 10 shows the distribution of the computed turbulent kinetic energy k. Figure 10a depicts a strong imbalance of the TKE between both slots. In the slot near the inflow duct significantly higher levels of turbulence occur. The TKE in the outlet section, shown in Figure 10b, reaches to a maximum of $k_{\text{max},y=0} = 2.11\,\text{m}^2/\text{s}^2$ with its average at $k_{\text{avg},y=0} = 1.06\,\text{m}^2/\text{s}^2$. The overall distribution is also nearly symmetric along the x-axis.

In both slots, the field smoothens towards the edges of the slots. Near the end of the slots ($|z| \gtrsim 470\,\text{mm}$) the influence of the wall becomes more prominent and causes another distortion of the flow field. In particular, we observe a sharp drop in velocity in the outer corners of the slots, which is accompanied by higher values of TKE.

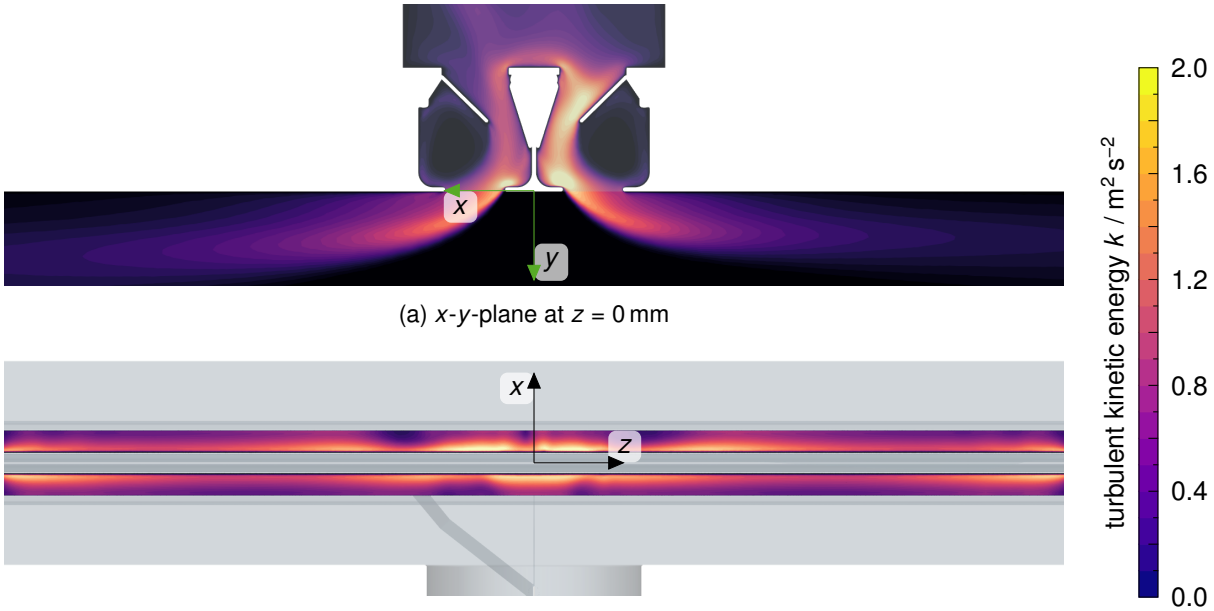

(a) x-y-plane at z = 0 mm

(b) x-z-plane at y = 0 mm

Figure 10: Computed distribution of the turbulent kinetic energy for v_D = 6 m/s

3.2. Broadband noise

In order to identify the regions where high levels are present and therefore identify the most noisy geometric features, we discuss the results of the two broadband noise source models. Figure 11 shows the distribution of the surface acoustic power which was computed with Curle's model. To allow for a better visualisation the model is clipped on a x-y-plane at z = 0 mm. Observing the diffuser from below (see Fig. 11a), different areas of high power levels are visible than from above (see Fig. 11b). The highest power levels are marked in the figures. Due to the dB-scale, it becomes clear that the edges contribute noise that is of several magnitudes stronger than the noise originating from the walls on the short edge (marked with 46 dB).

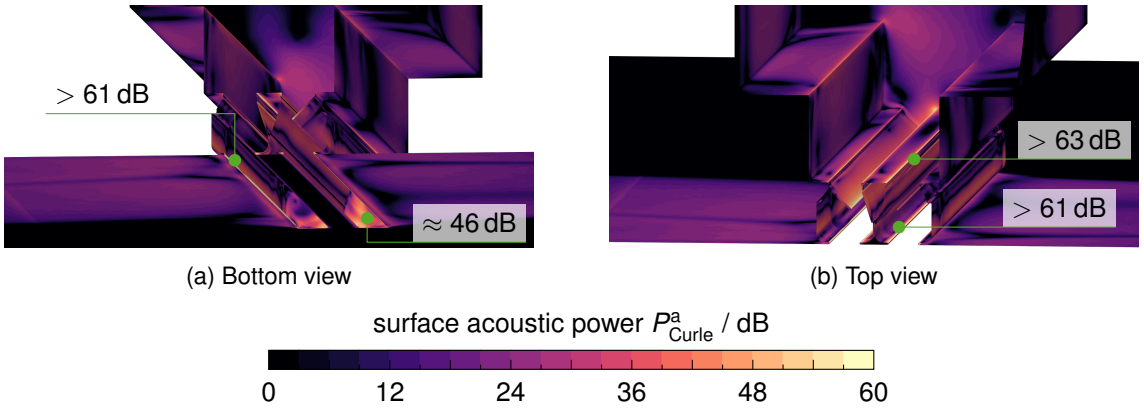

(a) Bottom view

(b) Top view

Figure 11: Distribution of surface acoustic power according to Curle's model for v_D = 6 m/s

Although Proudman's model depends primarily on the turbulent kinetic energy k, which is not fully valid in the simulations, we still give an impression of the according results in Figure 12. When comparing the distribution of the TKE and P^a_P, the relation becomes obvious. Even if we consider that our model presumably underpredicts the turbulence by a factor of $2-3$, the predicted noise levels according to Proudman's model would be of several magnitudes smaller than the levels predicted by Curle's model. Therefore the contribution of freestream turbulence to the overall noise emissions can be neglected.

Tables 4 and 5 list the integral values for both broadband noise models and all investigated velocities. Across all investigated diffuser velocities the general trends are the same, indicating that the influence of varying flow velocities mainly affects the overall level of emitted sound, rather than the aeroacoustic characteristics of the diffuser itself. Therefore, we again focus only on the medium velocity for a more detailed discussion.

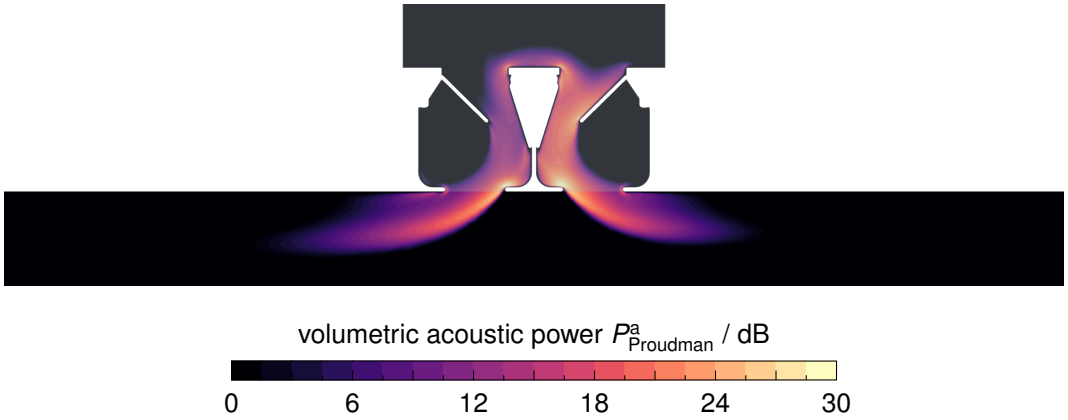

Figure 12: Distribution of volumetric acoustic power according to Proudman's model on a x-y-plane at $z = 0$ mm for $v_D = 6\,\mathrm{m/s}$

Table 4: Aeroacoustic results for Curle's model

Boundary	$P_{ac,Curle}$ / dB		
	4 m/s	6 m/s	8 m/s
Throttle	23.28	40.20	52.08
Flaps	61.93	79.80	92.48
Guides	66.81	86.25	99.82
Total	73.50	92.29	105.47

Table 5: Aeroacoustic results for Proudman's model

Volume	$P_{ac,Proudman}$ / dB		
	4 m/s	6 m/s	8 m/s
Plenum Box	–82.08	–48.72	–26.69
Outlet	–65.37	–32.92	–11.02
Room	–68.16	–36.01	–12.63
Total	–58.72	–26.29	–3.79

As we could already observe from the surface distribution (see Fig. 11) the *Flaps* and *Guides* contribute the most to the overall noise emission. Although the *Throttle* also has considerable emissions, it is neglectable compared to the other two surface groups. As already said, the emissions predicted by Proudman's model are neglectable compared to Curle's noise emissions. However we can note, that the increase of $P_{ac,Proudman}$ with rising diffuser velocity is greater than $P_{ac,Curle}$. This aligns with literature ([3, 8, 10]), where the acoustic power is theoretically derived to be dependent on the Mach number $M = \frac{v_D}{c}$.

$$P^{a}_{Curle} \propto M^3 \tag{20}$$

$$P^{a}_{Proudman} \propto M^5 \tag{21}$$

As our results show, the geometric features mainly responsible for acoustic emissions, are the edges in the diffuser plate region. In order to significantly reduce the noise of this particular diffuser, we propose design changes to these edges. Possible alterations may depend on if an edge is of the type of a leading or a trailing edge. Other researches already developed many measures to improve the aeroacoustic behaviour of such edges, which is why we just give a few examples. Gruber et al. [4] and Clark et al. [1] investigated the impact of trailing edge serrations. To improve the behaviour of a leading edge, Hansen et al. [5] added sinusoidal tubercles.

4. Conclusion

In this study, we presented a flow simulation of a two-slot air diffuser to predict areas of high noise emission for three diffuser velocities. By conducting flow measurements with a 3D-LDA system, we successfully validated the flow simulation in regards to velocity field and pressure loss. The computed turbulent kinetic energy is not only lower than measured, but we also observed strong anisotropy in the measured turbulence. However, under the investigated flow conditions, the contribution of freestream turbulence to the noise emission can be neglected. Therefore, the presumably under-predicted TKE does not appear to be relevant to the overall results. This leads us to the conclusion, that our flow model allows an accurate prediction of the most relevant regions responsible for noise emission. The main contributors are edges located in areas of high flow velocity. Both leading and trailing type edges emit noise of roughly equal strength.

There are various measures that can be taken to reduce noise emissions attributed to flow edges, depending on whether the edge being considered is a leading or trailing edge. In further studies these measures can be analysed regarding their influence on the noise emissions.

Acknowledgments

This project was funded by the AiF (Arbeitsgemeinschaft industrieller Forschungsvereinigungen) and the German Federal Ministry for Economic Affairs and Climate Action (BMWK) based on a resolution of the German Bundestag (IGF No.: 21611 N/1).

The authors gratefully acknowledge the computing time provided to them at the NHR Center NHR4CES at RWTH Aachen University (project number p0020083). This is funded by the Federal Ministry of Education and Research, and the state governments participating on the basis of the resolutions of the GWK for national high performance computing at universities (www.nhr-verein.de/unsere-partner).

References

[1] Ian A. Clark, W. Nathan Alexander, S. Devenport, W. und Glegg, C. Jaworski, J. W. und Daly, and N. Peake. Bioinspired Trailing-Edge Noise Control. *AIAA Journal*, 55(3):740–754, 2017. ISSN 0001-1452. doi: 10.2514/1.J055243.

[2] N. Curle. The mechanics of edge-tones. *Proceedings of the Royal Society of London. Series A. Mathematical and Physical Sciences*, 216(1126):412–424, 1953. ISSN 0080-4630. doi: 10.1098/rspa.1953.0030.

[3] N. Curle. The influence of solid boundaries upon aerodynamic sound. *Proceedings of the Royal Society of London. Series A. Mathematical and Physical Sciences*, 231(1187):505–514, 1955. ISSN 0080-4630. doi: 10.1098/rspa.1955.0191.

[4] Mathieu Gruber, Phillip Joseph, and Tze Chong. On the mechanisms of serrated airfoil trailing edge noise reduction. In *17th AIAA/CEAS Aeroacoustics Conference (32nd AIAA Aeroacoustics Conference)*, Reston, Virigina, 2011. American Institute of Aeronautics and Astronautics. ISBN 978-1-60086-943-3. doi: 10.2514/6.2011-2781.

[5] Kristy L. Hansen, Richard M. Kelso, and Bassam B. Dally. Performance Variations of Leading-Edge Tubercles for Distinct Airfoil Profiles. *AIAA Journal*, 49(1):185–194, 2011. ISSN 0001-1452. doi: 10.2514/1.J050631.

[6] Julius Oscar Hinze. *Turbulence*. McGraw-Hill series in mechanical engineering. McGraw-Hill, New York, NY, 2. edition, 1975. ISBN 0070290377.

[7] A. N. Kusyumov, S. A. Mikhailov, L. I. Garipova, A. S. Batrakov, and G. Barakos. Distribution of acoustic power spectra for an isolated helicopter fuselage. *EPJ Web of Conferences*, 114, 2016. doi: 10.1051/epjconf/201611402062.

[8] M. J. Lighthill. On sound generated aerodynamically i. general theory. *Proceedings of the Royal Society of London. Series A. Mathematical and Physical Sciences*, 211(1107):564–587, 1952. ISSN 0080-4630. doi: 10.1098/rspa.1952.0060.

[9] Philipp Ostmann, Christian Bruchhaus, Martin Kremer, and Dirk Müller. Numerische untersuchung des aeroakustischen verhaltens eines generischen schlitzauslasses. In *Fortschritte der Akustik - DAGA 2022*, pages 875–878, 2022.

[10] I. Proudman. The generation of noise by isotropic turbulence. *Proceedings of the Royal Society of London. Series A. Mathematical and Physical Sciences*, 214(1116):119–132, 1952. ISSN 0080-4630. doi: 10.1098/rspa.1952.0154.

[11] Asvath Ravichandran, Andreas Logdesser, Nikolaus Peller, and Michael Manhart. Experimentelle und numerische untersuchung des effekts der zuströmbedingungen auf die schallabstrahlung eines generischen ausströmers. In *Fortschritte der Akustik - DAGA 2022*, pages 1250–1253, 2022.

[12] Siemens. *STAR-CCM+ v. 17.06.008 UserGuide*, 2022.

[13] Matthias Tautz. *Aeroacoustic Noise Prediction of Automotive HVAC Systems*. Dissertation, FAU University, Erlangen, 2019.